First-Principle Molecular Dynamic Simulations along the Intrinsic Reaction Paths

Artur Michalak[†,‡] **and Tom Ziegler***[,†]

Department of Chemistry, University of Calgary, University Drive 2500, Calgary, Alberta, Canada T2N 1N4, and Department of Theoretical Chemistry, Faculty of Chemistry, Jagiellonian University, R. Ingardena 3, 30-060 Cracow, Poland

Received: November 9, 2000; In Final Form: February 8, 2001

Presented is an algorithm for performing the ab initio molecular dynamic (MD) simulations along the predetermined intrinsic reaction paths (IRP). The proposed approach has been implemented within the projector-augmented-wave DFT methodology (PAW program). The slow-growth MD simulations along the IRP has been applied for the reactions of (i) the HCN → CNH isomerization reaction, (ii) the conrotatory ring opening of cyclobutene, (iii) the prototype SN2 reaction $Cl^- + CH_3Cl \rightarrow ClCH_3 + Cl^-$, and (iv) the chloropropene isomerization $Cl{-}CH_2{-}CH{=}CH_2 \rightarrow CH_2{=}CH{-}CH_2Cl$. The results show that the slow-growth MD approach along the predetermined IRP leads to smooth free-energy profiles; use of a well-defined reaction coordinate (RC) reduces the problem of the free-energy hysteresis. Thus, the slow-growth simulations along the IRP typically require less time steps than the standard approach with an a priori chosen RC. The illustrative examples show that the applied methodology works well for the reactions involving concerted changes in many geometrical variables as well as in the cases when the finite-temperature paths strongly deviate from the IRP.

Introduction

Since the time of the original Car−Parinello article,[1] density functional theory (DFT)-based molecular dynamics (MD)[1,2] has established itself as a valuable and powerful tool in studies of chemical processes. A wide range of applications[2] starts from the studies of simple chemical reactions, and covers the areas of surface science and catalysis, material science, properties of liquids, glasses, and amorphous systems, as well as biochemistry. Recent applications of MD methodologies in chemical catalysis[3,4] include real-time reaction simulations,[5] studies of subpicosecond fluxionality,[6,7] reaction path scans,[8−12] and the free-energy calculations.[12−14] It has also been demonstrated that the Car-Parinello ab initio molecular dynamics can lead to a discovery of novel reaction pathways.[15] Recent examples also show that this approach can already be successfully applied to relatively large molecular systems, such as biologically active compounds,[16−19] or the real intermediates in olefin polymerization processes, involving catalyst-counterion ion pairs.[20] Implementations of the hybrid quantum-mechanics-molecular-mechanics (QM/MM) approaches[3,21,22] and the solvation models open ways toward exploring even larger and more realistic models of reactive systems.

One of the main advantages of the MD over the static quantum chemical approaches is that it can be utilized to directly determine the reaction free-energy barriers, as it explicitly includes entropic effects. An estimation of the free energy via a normal (static) DFT approach requires frequency calculations, relatively expensive for large molecular systems, and assumes harmonic (normal mode) approximation, which breaks down for processes where weak intermolecular forces dominate.[23]

Various methodologies have been developed to calculate free energy barriers from MD simulations. One of the common approaches applied in the ab initio MD, known as the potential of mean force method has been derived from the thermodynamic integration technique.[24,25] In a canonical (NVT) ensemble, the free energy difference ΔA between the two states **0** and **1** can be calculated as the integral

$$\Delta A_{(0\rightarrow 1)} = \int_0^1 \frac{\partial A(\lambda)}{\partial \lambda} d\lambda = \int_0^1 \left\langle \frac{\partial E(\mathbf{X}, \lambda)}{\partial \lambda} \right\rangle_\lambda d\lambda \qquad (1)$$

where the parameter λ is smoothly changing between the two states, E stands for the potential energy, and $\mathbf{X}$ denotes the coordinates of the atoms, $\mathbf{X} = \{X_i, i = 1, ..., 3N\}$; the subscript λ represents an ensemble average at fixed λ.

In practical applications, λ corresponds to an arbitrarily chosen reaction coordinate, defining the constraint in the configurational space; the constrained dynamics[26] at the finite temperature can be performed for a series of fixed λ values and the free energy can be calculated as

$$\Delta A = \sum_i^{n_{\text{points}}} \langle F_i \rangle_\lambda \, \Delta\lambda_i \qquad (2)$$

where F_j denotes the force required to satisfy the constraint corresponding to λ_j. In such an approach the system must be properly equilibrated for each λ_j and the simulation must be continued for a long enough period to obtain an adequate value of the average force F_j.

Alternatively in a *slow-growth* approach[27] the constraint value is changed in a continuous manner from the initial to the final state. Thus, the thermal equilibration of the system must be performed at the initial state only. If the rate of the constraint change is small, the system may stay (approximately) equilibrated during the simulation.

However, the reaction barriers obtained from thermodynamic integration in slow-growth simulations are dependent on the

* To whom correspondence should be addressed.
† Department of Chemistry.
‡ Department of Theoretical Chemistry.

10.1021/jp0041297 CCC: $20.00
Published on Web 04/11/2001

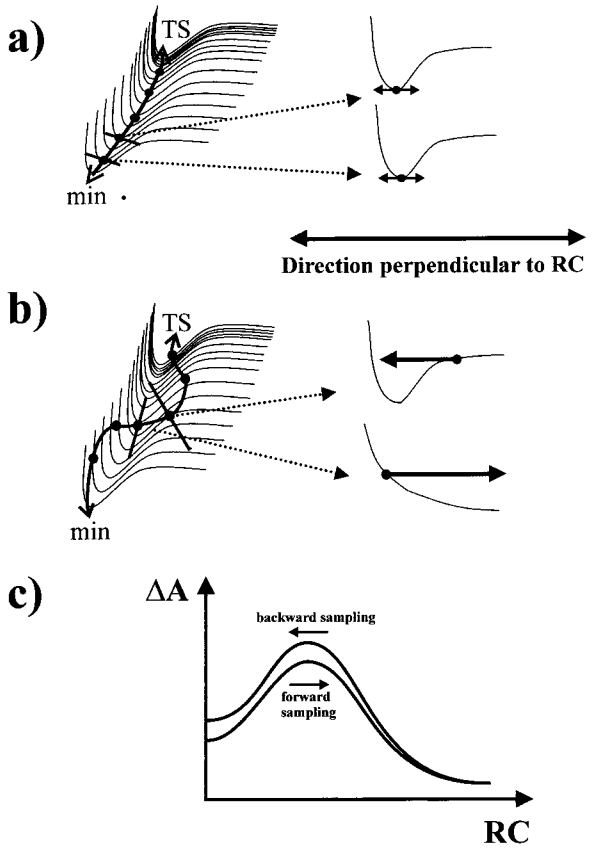

Figure 1. Implications of the reaction coordinate choice for MD simulations. In part a the assumed reaction path goes along the bottom of a valley connecting TS and the reactants/products, and the shape of the potential energy cut in the direction perpendicular to RP changes smoothly, when changing points on RP. RP of part b crosses the bottom of the valley, and the system easily loses equilibration as a result of the large changes of the potential energy shape in the perpendicular direction. In part c a hysteresis in the free energy profile is shown.

choice of the reaction coordinate. First of all, an unfortunate choice of the reaction coordinate may correspond to an unfavorable reaction path, which does not pass the transition state region, and may lead to substantial overestimation of the barrier.

Further, even if the reaction path goes trough the transition state, a large hysteresis[3] in the free energy profile can be observed. This can happen if the RP does not run along, but crosses the bottom of the valley connecting the transition states with reactants/products. We schematically illustrate this problem and its source in Figure 1. Note that at fixed values of the reaction coordinate, the system is allowed to evolve in all the directions perpendicular to the corresponding reaction path. If, as in part a of the figure, the reaction path goes along the bottom of the valley and the reaction coordinate is changed slowly, the cut of the potential energy surface in the perpendicular direction practically does not change for the two consecutive points on the RP. Thus, the system regularly oscillates around the minimum and stays equilibrated during the whole simulation.

If the reaction path crosses the bottom of the valley (Figure 1b), however, the projection of the gradient on the direction perpendicular to the RP can be substantial for some points. Thus, for such points the fixed constraint value does not prevent the system from "sliding" downhill the potential energy surface. In other words, the cut of the potential energy surface in the direction perpendicular to the RP may change dramatically for the two consecutive points on the RP. For example, with the constraint defined by a reaction path shown in Figure 2b, from the point A the system will spontaneously evolve toward the TS, while from the point B toward the minimum. Eventually, the system can easily loose its equillibration as a result of "chaotic" movements following the change in the constraint value. This leads to a hysteresis in the free energy profile for a forward and backward scan (part c). It should be pointed out, however, that for an infinite sampling, i.e., infinitesimal change in the constraint value, the hysteresis problem will usually disappear.

In practical applications the reaction coordinate is usually chosen as a single geometrical variable (bond length, bond, angle, or torsion angle) or a simple combination of few variables. Except for the simplest reactions, such an a proiri choice of the reaction coordinate cannot guarantee that the RP reaches the true TS region nor that it goes along the bottom of the valley connecting TS with the reactants/products. In the following we propose an a posteriori approach, in which the finite temperature MD simulations are performed along the predetermined reaction paths.

The *intrinsic reaction path* (IRP) of Fukui[28,29] has been chosen here, since by definition it goes along the bottom of the valley connecting the TS with reactants/products. As such, the IRC has been used as a reference path in the methods of the dynamic reaction paths analysis.[30]

The IRP has been defined by the equation

$$dx_i = -\frac{\partial \mathbf{E}}{\partial x_i} dt \tag{3}$$

where x_i stands for the mass-weighted Cartesian coordinates:

$$x_i = \sqrt{m_i}\, X_i \; i = 1, ..., 3N \tag{4}$$

and m_i corresponds to the atomic mass of the atom with a position described by the ith coordinate. Thus, the IRP simply corresponds to a steepest descent path in a mass-weighted coordinates.

In the following section we will present the proposed algorithm, followed by the computational details. The four illustrative examples include the HCN → CNH isomerization reaction, the conrotatory ring opening of cyclobutene, the prototype SN2 reaction, $Cl^- + CH_3Cl \rightarrow ClCH_3 + Cl^-$, and the chloropropene isomerization, $Cl{-}CH_2{-}CH{=}CH_2 \rightarrow CH_2{=}CH{-}CH_2Cl$. The first three of the above reactions has been used as routine test cases for methods of determining the IRP in the static quantum chemical calculations.[31−38] As will be shown, the last reaction in the list, the chloropropene isomerization, represents an interesting example of the system for which MD reveals a "thermal shortcut", i.e., the 300 K path does not follow the zero-temperature IRP, leading directly to a different, more stable conformer.

Methodology and Computational Details. Let us assume that for the given chemical reaction the intrinsic reaction path is known, and discretized by the set of the k points in the configurational space, i.e., by the set of k molecular geometries:

$$\boldsymbol{X}^{j,\mathrm{IRP}} = \{X_i^j;\, i = 1, ..., 3N\},\, j = 1, ..., k \tag{5}$$

or in mass-weighted coordinates

$$\boldsymbol{x}^{j,\mathrm{IRP}} = \{\sqrt{m_i}\, X_i^j;\, i = 1, ..., 3N\}, \quad j = 1, ..., k \tag{6}$$

To fix the molecular system at the jth point on the reaction path, the following constraint must be used in mass-weighted

coordinates:

$$(\boldsymbol{x} - \boldsymbol{x}^{j,\mathrm{IRP}}) \cdot \boldsymbol{g}^{j,\mathrm{IRP}} = 0 \quad (7)$$

i.e., the projection of actual atomic position vector $\boldsymbol{x}$ on the gradient direction $\boldsymbol{g}^{j,\mathrm{IRP}}$ must be constant and equal to the corresponding value for the IRP geometry $\boldsymbol{x}^{j,\mathrm{IRP}}$. Obviously, from the definition of the IRP (eq 3) the gradient direction is given by the (normalized) difference in the two IRP geometries:

$$\boldsymbol{g}^{j,\mathrm{IRP}} = N^j \Delta \boldsymbol{x}^{j,\mathrm{IRP}} = N^j(\boldsymbol{x}^{j+1,\mathrm{IRP}} - \boldsymbol{x}^{j-1,\mathrm{IRP}}) \quad (8)$$

with normalization factor N^j.

In practical applications it may be more convenient to apply the constraint in Cartesian space, instead of mass-weighted space. Thus, the atomic positions $\boldsymbol{X}$ must satisfy the corresponding linear constraint:

$$(\boldsymbol{X} - \boldsymbol{X}^{j,\mathrm{IRP}}) \cdot \boldsymbol{G}^{j,\mathrm{IRP}} = 0 \quad (9)$$

where

$$\boldsymbol{G}^{j,\mathrm{IRP}} = \{N^j m_i \Delta X_i^{j,\mathrm{IRP}}\} = \{N^j m_i (X_i^{j+1,\mathrm{IRP}} - X_i^{j-1,\mathrm{IRP}}), \quad i = 1, ..., 3N\} \quad (10)$$

In our approach we perform the MD simulations along the IRP with the linear constraint of eq 9. In the slow-growth simulations, the constraint is smoothly changed for every time step, on the basis of the knowledge of the points on the predetermined IRP. For every time step, the force F^j, required to satisfy the constraint is calculated, and finally the free energy, is obtained as

$$\Delta A = \sum_j^{n_{\mathrm{steps}}} F^j \Delta s^j \quad (11)$$

where Δs^j corresponds to the change in the constraint value for the jth point

$$\Delta s^j = \frac{1}{2}[(\boldsymbol{X}^{j+1,\mathrm{IRP}} \cdot \boldsymbol{G}^{j,\mathrm{IRP}}) - (\boldsymbol{X}^{j-1,\mathrm{IRP}} \cdot \boldsymbol{G}^{j,\mathrm{IRP}})] \quad (12)$$

All reported numerical results were obtained with the Car-Parrinello projector augmented wave (PAW) code developed by Blöchl.[39,40] The wave function was expanded in plane waves up to an energy cutoff of 30 Ry. The frozen core approximation has been employed; a Ne core has been used for Cl, and a He core for the first-row elements. Periodic boundary conditions were used, with a unit cell spanned by the lattice vectors ([0 7 7] [7 0 7] [7 7 0]) (Å). All simulations were performed using the local density approximation in the parametrization of Perdew and Zunger[41] with gradient corrections due to Becke and Perdew.[42−44] To prevent electrostatic interactions between neighboring unit cells, the charge isolation scheme of Blöchl was used.[40] To achieve an evenly distributed thermal excitation, the nuclei were brought to a temperature of 300 K by applying a sequence of 30 sinusoidal pulses, each of which was chosen to raise the temperature by 10 K. Each of the excitation vectors was chosen to be orthogonal to the already excited modes. The warmed-up systems were equilibrated for the 10 000 time steps. The time step of 7 au was used. Constraints were maintained by SHAKE algorithm.[26] A temperature of 300 K was controlled by a Nosé thermostat, which creates a canonical (NVT) ensemble.[45,46] The fictitious kinetic energy of the electrons was controlled in a similar fashion by a Nosé thermostat.[47]

Prior to MD simulations, the transition state (TS) structures were determined by the method described by Blöchl.[48] The intrinsic reaction paths were determined by the steepest descent in mass-weighted coordinates going from the TS to the reactants and products; this corresponds to a 0 K simulations with a friction coefficient of 1.0. To increase the efficiency of the IRP determination, the nuclear displacements were scaled up by a factor of 2.0, until the average displacement in the geometry reached a value of 0.001 Å or an increase in the potential energy was noticed. The slow-growth MD simulations were performed with a constraints of eq 9, for the equidistant points on the IRP, with an increment of 0.0002 amu$^{-1/2}$ bohr at every time step. This corresponds to a total number of 39300, 66450, 22600, and 55300 time steps for simulations of the HCN → CNH isomerization, ring opening of cyclobutene, SN2 reaction, and the chloropropene isomerization, respectively. In the case of the last two reactions, due to symmetry, only the paths leading from TS to the products were studied.

Results and Discussion

A. HCN → CNH Isomerization. The isomerization of hydrogen cyanide to hydrogen isocyanide has been extensively studied by both experimental and theoretical methods.[49−55] This reaction has also been widely used as a test case for the IRP determination methods.[31−36] Figures 2 and 3 summarize the results of our calculations. Since the detailed comparison of the results obtained with different theoretical techniques has been published elsewhere, we will not compare our results with those obtained with all the other methods here. A discussion will be restricted to a comparison with recant static nonlocal DFT calculation[35,36] and the experimental data.[55]

The structures of HCN, triangular TS, and CNH are shown in Figure 2a. The IRC energy profile is shown in Figure 2b; the free energy profile together with the average potential energy profile obtained from the MD simulations at 300 K are presented in Figure 2c. The average potential energy in Figure 2c has been calculated as running average with the window of 200 time steps. The portion of the IRP from HCN to TS is shorter than the path from TS to CNH, with lengths of IRP $s = 3.58$ and $s = 4.28$ amu$^{-1/2}$ bohr, respectively. From our calculations the reaction is endothermic with $\Delta E = +14.0$ kcal/mol. This is slightly smaller than the static DFT value[35,36] of 15.4 kcal/mol obtained with the VWN LDA + BP86 exchange correlation functional, with the atom-centered Slater basis sets. Similarly, the reaction barrier of 44.7 kcal/mol from present calculations is smaller than the previous[35,36] DFT result of 45.9 kcal/mol. The average potential energy profile of Figure 2c is practically indistinguishable from the IRC profile, within the accuracy of 0.1 kcal/mol. The reaction free energy, $\Delta A = 14.1$ kcal/mol, and the reaction free energy barrier, $\Delta A^{\#} = 44.6$ kcal/mol are almost identical to the zero-temperature ΔE values. These values are in a good agreement with experimental results of the reaction energy. The experimental estimates[56] vary between 10.8 and 14.8 kcal/mol; the most recent value[55] is 14.8 ± 2 kcal/mol. We would like to point out here that the zero-point energy correction is not taken into account in our calculations. In the previous calculation[35,36] this correction has been estimated to be placed between −0.1 and −1.0 kcal/mol for the reaction energy, and between −2.4 and −4.0 kcal/mol for the reaction barrier.

In Figure 2e the changes in the interatomic distances along the IRP are presented, while Figure 2f shows the corresponding changes during the 300 K MD simulation along the IRP. The geometries of the reactant, product and the TS are practically

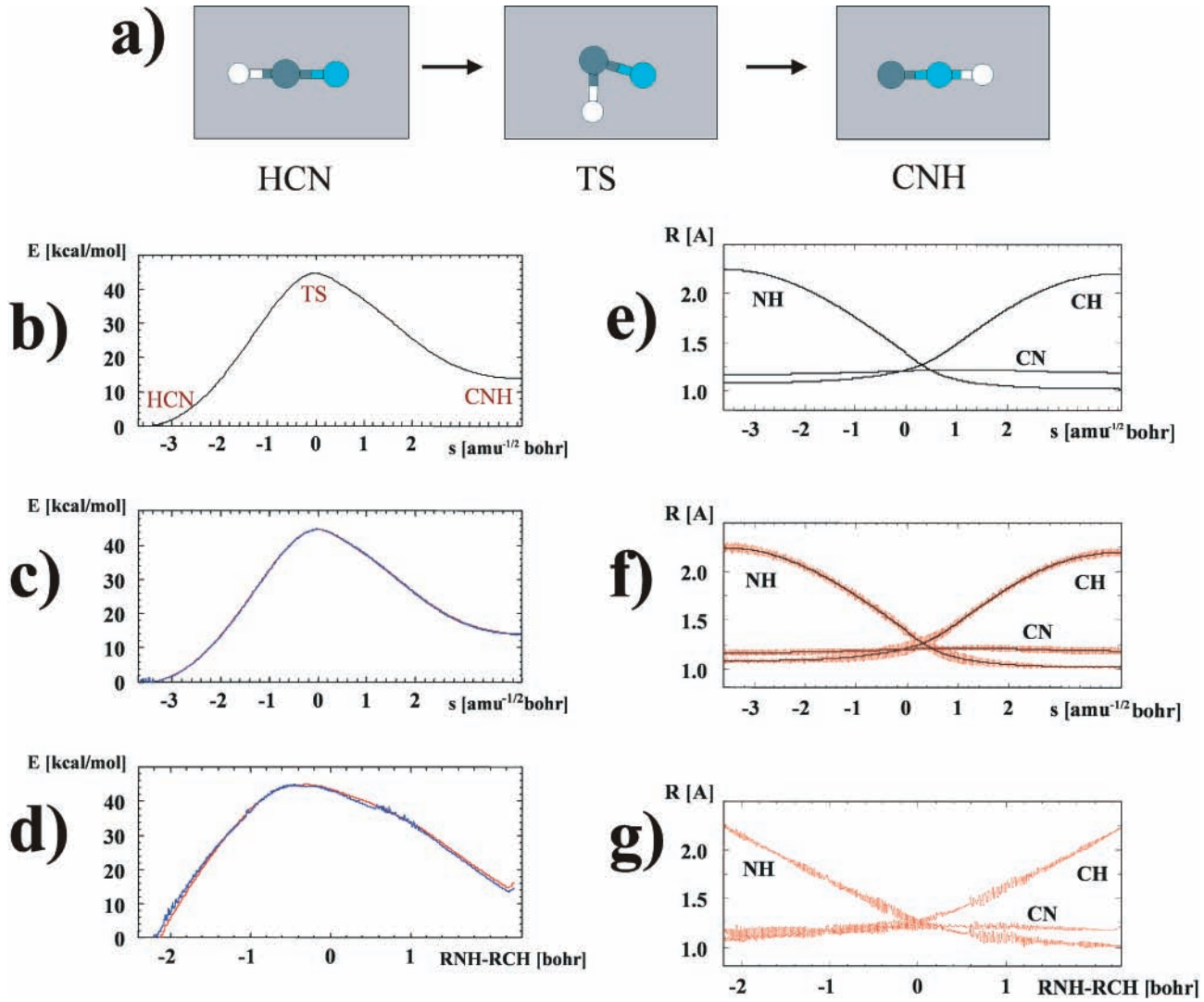

Figure 2. Isomerization of hydrogen cyanide to hydrogen isocyanide. The structures of the reactant, TS, and the product are shown in part a. The IRC energy profile is shown in part b. In parts c and d presented are the free-energy profiles (red lines) and the average potential energy profiles (blue lines), calculated from the 300 K MD simulations along the IRP and from the 300 K MD simulation with the constraint $R_{NH} - R_{CH} = \text{const.}$, respectively. Parts e, f, and g present the changes in CH, NH, and CN distances along the IRP, during the 300 K MD simulations along the IRP and during the 300 K MD simulation with the constraint $R_{NH} - R_{CH} = \text{const.}$, respectively.

identical (within 0.005 Å) with both, the previous static DFT calculations[35,36] and the experimental data.[56] For HCN the CN, CH, and NH distances are 1.16, 1.08, and 2.25 Å, respectively; the corresponding values for the CNH molecule and the TS are 1.17, 2.20, 1.01 Å, and 1.20, 1.21, 1.38 Å, respectively. Figure 2f demonstrates that during the simulation all geometrical parameters regularly oscillate around the IRP values. The CN distance changes by ±0.05 Å in the HCN region, while in the TS region and CNH region by ±0.02 and ±0.03 Å, respectively. The CH distance varies by ±0.03 Å in the HCN region and by ±0.07 and ±0.05 Å in the TS and CNH region, respectively. The NH distance oscillates with the amplitude of ±0.02, ±0.06, and ±0.05 Å in the CNH, TS, and CNH regions, respectively. The changes in the amplitudes of vibrations in different regions on the reaction path reflect the trends observed in the vibrational frequencies. Namely, the CN stretching mode has higher frequency for the HCN molecule than for CNH; the experimental values are 2129 and 2067 cm^{-1}, respectively.[56] Similarly, the CH stretching mode in HCN has lower frequency than the NH stretching mode in CNH; the experimental values are 3442 and 3842 cm^{-1}, respectively.[56]

Let us now compare the results of the MD along the IRP with the similar simulations performed with the a priori assumed reaction coordinate. Here we chose the difference between NH and CH distances as a reaction coordinate, i.e., with the substitution constraint, $R_{NH} - R_{CH} = \text{const}$. The slow-growth MD simulation was performed with the same number of time steps and the same details of the computations, as the simulations along the IRP; the constraint value was smoothly changed between the values in the HCN and CNH molecules. The free energy profile as the function of the assumed RC, and the average potential energy are plotted in Figure 2d. The CN, CH, and NH distances from this simulation are presented in Figure 2g.

The plot in Figure 2d indicate there are pronounced difference between the ΔA and $\langle \Delta E \rangle$ profiles. Unlike in the simulation along the IRP, the free energy profile crosses the average potential energy curve. Although the reaction barrier practically does not differ from the value obtained from the simulation along IRP, the reaction free energy is higher by ca. 1.2 kcal/mol than the change in the average potential energy between HCN and CNH. Figure 2d also shows that the $\langle \Delta E \rangle$ profile exhibit larger irregularities, especially in the begining of the simulation ($R_{NH} - R_{CH} =$ from −2.1 to −1.8) and in the region

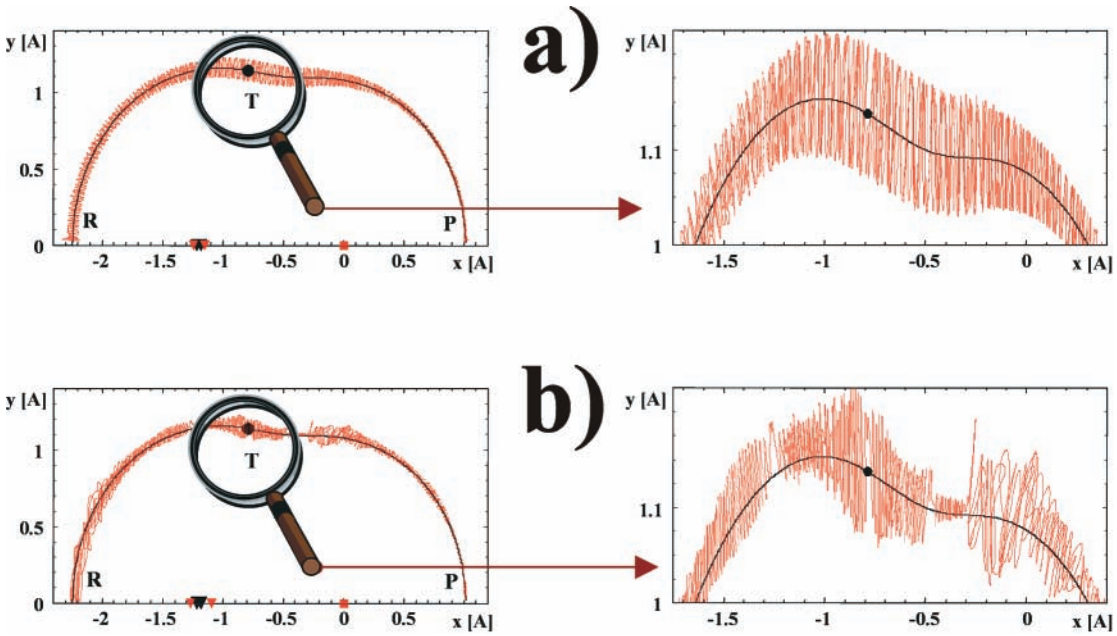

Figure 3. Relative motion of the atoms during the isomerization of hydrogen cyanide to hydrogen isocyanide calculated from the 300 K MD simulations along the IRP (red in part a) and from the 300 K MD simulation with the constraint $R_{NH} - R_{CH} =$ const. (red in part b). The corresponding data along the IRP are shown in black. The position of the nitrogen atom, fixed at the origin (0,0), is represented by squares. The lines correspond to the trajectories of the hydrogen atom, while the triangles indicate two limiting positions of the carbon atom. The region closed to TS is magnified in the plots shown of the right.

after passing the TS ($R_{NH} - R_{CH} =$ from 0.6 to 1.2 bohr). In these regions the reaction path defined by the substitution constraint deviate from the IRC, and since the applied constraint does not represent the minimum energy path, the molecular system spontaneously evolve toward lower energies, partially loosing equilibration. This effect is especially pronounced in the region after TS, and reflected by the changes in interatomic distances of Figure 2g. After passing TS, the substitution constraint does not prevent going downhill the potential energy surface; this is reflected by dumped oscillations between the constraint values of 0.2 and 0.6 bohr. Afterward, inequilibrated systems exhibits increased variation in all the interatoomic distances between the constraint values of 0.6 and 1.2 bohr.

The effect discussed above is even more pronounced in Figure 3, in which we compare the hydrogen paths from the two simulations, plotted together with the hydrogen path corresponding to IRP. While the hydrogen path from the simulation along the IRP (Figure 3a) oscillates very regularly around IRP, in the case of the simulations with the substitution constraint (Figure 3b) strong irregularities can be observed. Here, after passing TS the oscillations are first dumped—the hydrogen atom runs away from the IRP, and then increased in a quite chaotic fashion—a sign that the system has lost its equilibration. In this simple reaction involving small, triatomic molecule, the problem discussed above does not affect the reaction free energy very much, since the molecule equilibrates back relatively quickly. In the large molecular systems with many degrees of freedom, however, the equilibration lost at some point can lead to inaccurate estimation of the reaction free energies as well as the reaction barriers.

B. Conrotatory Ring Opening of Cyclobutene. The reaction of cyclobutene ring opening leading to 1,3-cyclobutadiene was extensively studied by experimental and theoretical methods.[35,38,57−64] The theoretical results obtained by various methods have been reviewed and compared elsewhere;[35,38,64] here, we compare our results only with the recent, static DFT studies[35,38] and the experimental data.[57−60]

The ring opening of cyclobutadiene is predicted by symmetry rules to proceed as conrotatory process. The kinetic product of the reaction is gauche-1,3-butadiene with deviation from planarity of ca. 30°. The structures of the cyclobutene, TS, and gauche-1,3-butadiene are shown in Figure 4a. The kinetic product can be further transformed into the most stable trans- isomer. Here, we study only the pathway leading to a gauche rotamer. The mechanism of the reaction involves four main processes: (i) breaking of the C_1-C_4 σ-bond; (ii) rehybridiration of the carbon skeleton, i.e., formation of the conjugated π-electron system by partial breaking of the $C_2=C_3$ π-bond and partial formation of the $C_1=C_2$ and $C_3=C_4$ π-bonds; (iii) skewing of the carbon skeleton by rotation around C_2-C_3 bond; (iv) conrotatory movement of the two methylene groups. The recent static DFT IRC studies[35,38] demonstrated that the reaction proceeds in a concerned fashion rather than according to a stepwise mechanism. Since the reaction path involves concerned changes in all geometrical parameters, it represents an interesting test case for the MD along the IRP.

The results of our calculation are summarized in Figure 4. Let us first discuss the energetics of the reaction. The IRC energy profile together with a free energy profile from the MD simulations along the IRP are shown in Figure 4b. From our calculations the reaction energy is $\Delta E = -8.5$ kcal/mol, and the free energy $\Delta A = -8.0$ kcal/mol. These numbers are lower than the previous DFT result[35,38] for the reaction energy of −9.3 kcal/mol and the experimental value of -9.7 ± 0.4 kcal/mol.[64] The reaction barrier from our calculations is characterized by $\Delta E^{\#} = 30.9$ kcal/mol, and $\Delta A^{\#} = 31.0$ kcal/mol. Again, this values are slightly lower than the previous DFT (31.3 kcal/mol) and experimental result (32.8 ± 0.5 kcal/mol). The difference between present and the previous DFT estimates may be attributed to different methodologies used (augmented plane wave vs Slater TZ basis set). Here, we would like to point out an important result of our simulations. Namely, the MD simulation along the IRP leads to a very smooth free energy profile.

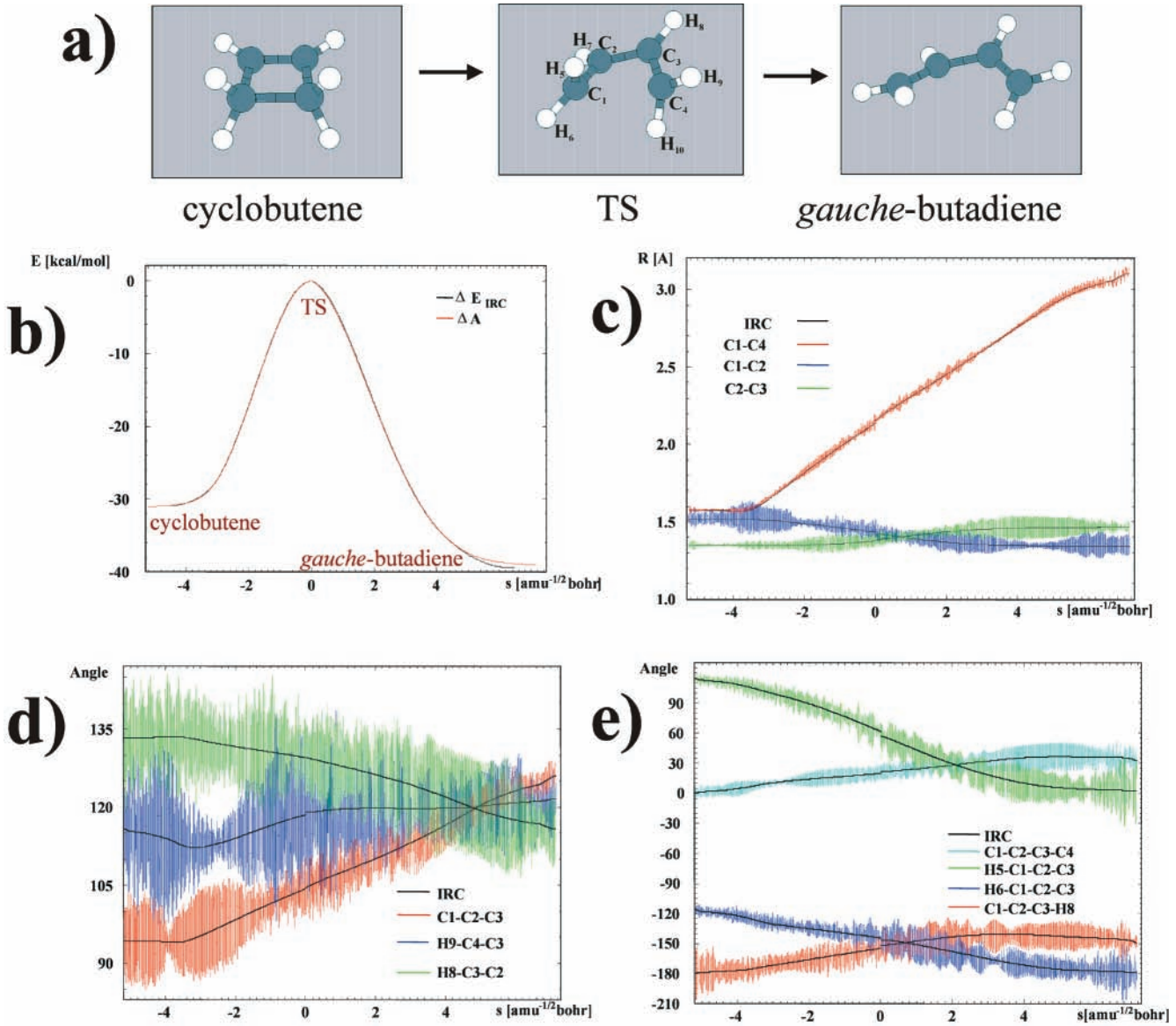

Figure 4. Conrotatory ring opening of cyclobutene. The reactant, TS, and the product are shown in part a. Part b presents the IRC energy (black line) and the free-energy (red line) profiles. The changes in the selected interatomic distances, bond angles, and dihedral angles are shown in parts c, d, and e, respectively; the black lines correspond to the changes along the IRP, while the color lines represent the changes during the 300 K MD simulation along the IRP.

In the remaining panels of the Figure 4 we present the changes in the selected interatomic distances, bond angles, and torsion angles during the 300 K MD simulation along the IRP (color lines), together with the IRP values (black lines). Similarly to the previous study of the IRP, the results obtained here suggest that the reaction proceeds according to a concerted mechanism. The C_1-C_4 bond breaking starts at $s = -3.8$ amu$^{-1/2}$ bohr, followed by a practically linear increase in the C_1-C_4 distance. The C_1-C_4 distance in cyclobutadiene, TS, and gauche-1,3-butadiene is 1.57, 2.145, and 3.10 Å, respectively. The first two numbers perfectly agree with the previous DFT results[35,38] and the experimental value[65] for cyclobutadiene. The third value (in gauche-1,3-butadiene) is lower than the previous result by 0.017 Å; the difference seems to be acceptable since it characterizes nonbonded distance. At 300 K the C_1-C_4 distance oscillates around the IRP value with an amplitude of ±0.05 Å along the whole reaction paths. The structure of the oscillations observed in Figure 4 comes from a coupling (resonance) between different geometrical parameters.

The rehybridization of the carbon skeleton to form the conjugated π-electron system is reflected by changes in the C_1-C_2 (or C_3-C_4) and C_2-C_3 distances. The change in these distances is only sligthly delayed in comparison to the σ-bond breaking: the C_1-C_2 length remains practically constant until $s = -3.6$, and the C_2-C_3 distance until $s = -2.0$ amu$^{-1/2}$ bohr. The C_1-C_2 distance in the substrate, TS, and the kinetic product is 1.52, 1.425, and 1.34 Å, respectively. The C_2-C_3 distance in cyclobutene, TS, and butadiene is 1.35, 1.38, and 1.47 Å, respectively. All this numbers compare well (within 0.01 Å) with the previous calculations[35,38] and the experimental data.[65] During the MD simulation both C_1-C_2 and C_2-C_3 oscillate around the IRP values with an amplitude up to ±0.1 Å.

The changes in the selected bond angles presented in the Figure 4d accompany the rehybridization of the carbon skeleton. The $C_1-C_2-C_3$ angle start changing practically since s = −3.6 amu$^{-1/2}$ bohr, so does the $H_8-C_3-C_2$ angle (and the equivalent $H_7-C_2-C_3$ angle). The values of the $C_1-C_2-C_3$ angle in the reactant, TS and product are 94, 104, 126°, respectively. The $H_8-C_3-C_2$ angle changes from 133° in cyclobutene, through 128° in TS, to the value of 116° in the product. The value for

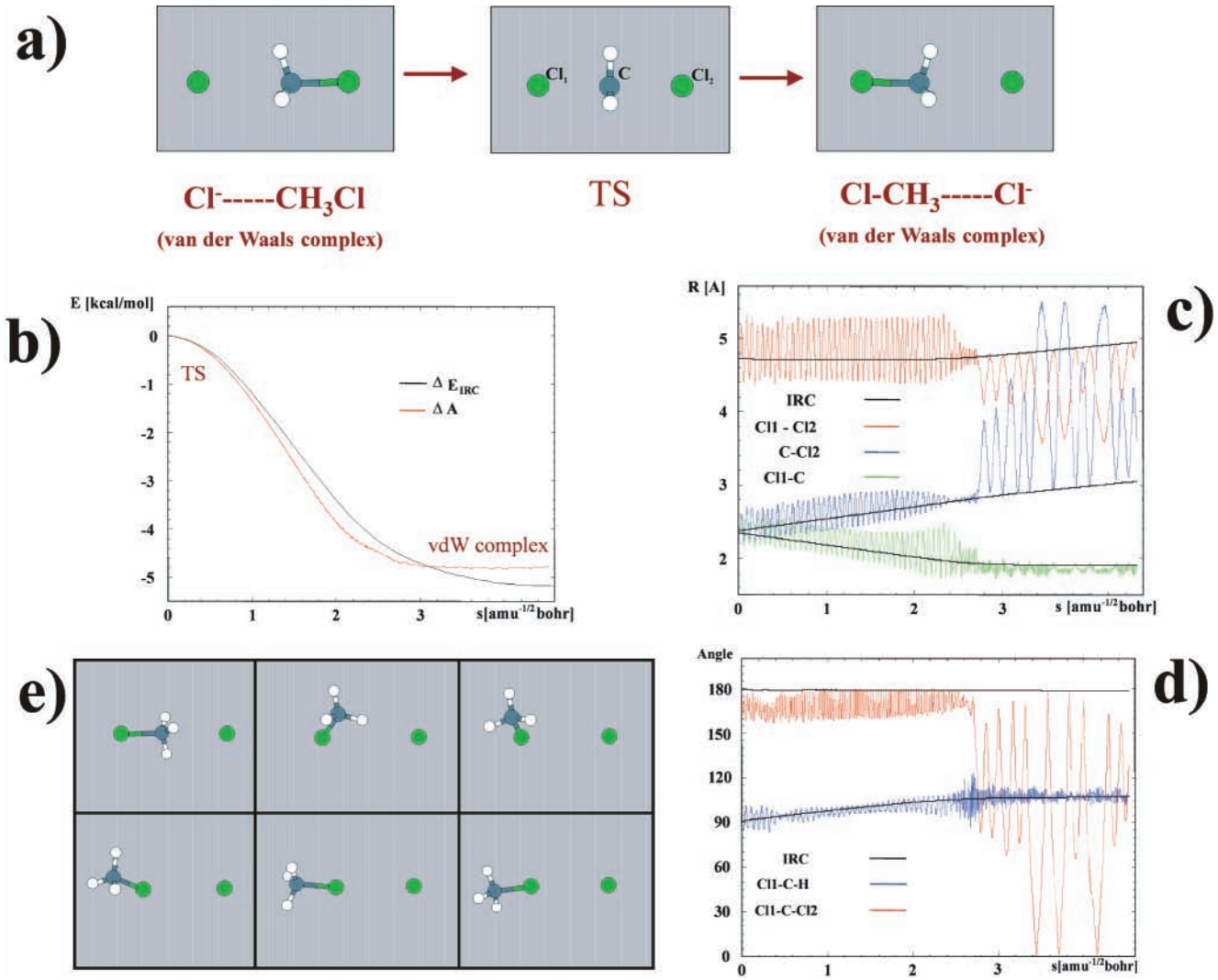

Figure 5. Prototype SN2 reaction. The reactant, TS, and the product are shown in part a. Part b presents the IRC energy (black line) and the free-energy (red line) profiles. The changes in the selected interatomic distances and the bond angles are shown in parts c and d, respectively; the black lines correspond to the changes along the IRP, while the color lines represent the changes during the 300 K MD simulation along the IRP. Selected geometries in the VdW complex region at 300 K are shown in part e.

the $H_9-C_4-C_3$ angle (and its three equivalents) of 115° is relatively large in a strained four-member ring of cyclobutene. In the IRP it initially decreases toward tetrahedrical value, when the cyclobutene ring becomes less strained as a result of initial rotation of the carbon skeleton around the C_2-C_3 bond, and then it increases as a result of rehybridization of the C_4 carbon atom. In the TS and the product the values of this angle are 119 and 121° , respectively. At 300 K all the angles oscillate around their IRP values quite regularly, with the amplitude of ±7−16°.

Finally, Figure 2e demonstrate that all the dihedral angles start changing practically from the begining of the reaction path. The $C_1-C_2-C_3-C_4$ angle corresponding to skewing the carbon skeleton changes from the value of 0° in the reactant, through 27° in TS to 33° in the product. The values of the $H_5-C_1-C_2-C_3$ angle, describing the rotation of the methylene group, in the reactant, TS and product are 115, 60, and 0°, respectively. During the finite temperature MD simulation the dihedral angles oscillate around the corresponding IRP values with an amplitude up to ±35°.

The example of the cyclobutene ring opening reaction demonstrate that the MD along the IRP leads to smooth free energy profiles even in the cases when the reaction involves concerted changes in many geometrical parameters. All the geometrical variables regularly oscillate around their IRP values and the system practically stays equilibrated during the whole slow-growth MD simulation.

C. Prototype SN2 reaction $Cl^- + CH_3Cl \rightarrow ClCH_3 + Cl^-$. The halogen exchange reactions between methyl halides and halogen anions, $X^- + CH_3X \rightarrow XCH_3 + X^-$, X = F, Cl, Br, and I, have been studied by many experimental and theoretical techniques as a prototype SN2 reaction.[35,37,66−92] In the present work we have studied the chlorine exchange reaction. Again, since the comparison of the results obtained with different methodologies has been presented elsewhere, a comparison will be limited to the recent static DFT IRC calculations.[35,37]

The reaction profile is characterized by a double-well shape with the two minima, corresponding to a van der Waals complexes (VdW), $X^-\cdots CH_3X$, located symmetrically around the barrier. In the present work we studied the major part of the reaction, i.e., the path between VdW complex and the TS; the reaction path corresponding to a formation of the VdW complex from the isolated chlorine anion and chloromethane has not been studied here. The structures of the two VdW complexes and the TS are shown in Figure 5a. Because of reactants−products symmetry, in the following we present the

results of the MD simulation along the part of the IRP leading from the transition state to a VdW complex.

The results of our simulation are summarized in Figure 5. Let us start a discussion with the energetics of the reaction. In Figure 5b the IRC energy and free energy profiles are presented. From our calculations the internal barrier of the reaction is characterized by $\Delta E^{\#} = 5.2$ kcal/mol, and $\Delta A^{\#} = 4.8$ kcal/mol. These results are slightly higher than the previous estimate of $\Delta E^{\#} = 4.6$ kcal/mol from static nonlocal DFT calculations.[35,37] Since we studied here only the part of the reaction path leading from the VdW complex, it is hard to compare our results with experimental data obtained from this reaction. A comparison between the previous static DFT calculation for the complete reaction and the experimental data has been presented elsewhere and revealed a good agreement.[35,37]

One feature of the profiles of Figure 5b is worth pointing out. Namely, while the energy decreases along the whole reaction path until the final geometry of the VdW complex, the free energy is practically constant in the final part of the reaction, for $s > 2.8$ amu$^{-1/2}$ bohr, i.e., after the C−Cl bond formation. We will discuss this later.

The changes in selected interatomic distances and angles from the 300 K MD simulation along the IRP are presented in Figure 5c,d. The reaction mechanism involves Walden inversion of chloromethane, with the planar CH_3 group in the symmetrical transition state geometry. The IRP involves linear movement of the carbon and two chlorine atoms, accompanied by bending the C−H bonds toward tetrahedrical orientation. The C−Cl bond lengths in transition state are 2.36 Å, while 1.89 (bonded C−Cl) and 3.05 Å (nonbonded C−Cl) in the VdW complex geometry. The corresponding values from the previous DFT calculations are 2.34, 1.84, and 3.09 Å. The distances between two chlorine atoms (sum of the two C−Cl distances) in the TS and VdW complex are 4.71 and 4.94 Å, respectively. For the VdW complex the difference between the present and previous studies is only 0.01 Å. Thus, in our present approach the bonded C−Cl distance seems to be overestimated and the nonbonded underestimated. This relatively large difference in the C−Cl distances at the VdW complex may be attributed to different methodologies, and especially to the difference between basis sets used (augmented plane waves vs atom centered TZ+2P Slater basis sets). The H−C−Cl angle along the IRP changes from 90° in TS to 107° in VdW geometry. This agrees quite well with the previous results of 90° and 107.9°.

At 300 K, in the TS region the atomic movements are dominated by two soft modes: the bending of the Cl−C−Cl angle, i.e., the movement of the CH_3 fragment perpendicular to the Cl−Cl axis, and the symmetrical stretching of the two C−Cl bonds. In the TS region the C−Cl distances changes with an amplitude of ±0.30 Å and maximal deviation of the Cl−C−Cl angle from the linear orientation is 24°. The plots of Figure 5c,d show that during the MD simulation all bonded interatomic distances oscillate around their IRP values with relatively small amplitudes. In the case of nonbonded distances, however, large deviations from their IRP values may be observed for the RC values corresponding to the reagion after C−Cl bond-formation, i.e., $s > 2.8$ amu$^{-1/2}$ bohr. This is because the dynamic VdW complex at 300 K does not resemble its static image at 0 K. After the formation of the C−Cl bond, the chloromethane molecule starts rotating. Thus, the Cl−C−Cl angle adapts values from the whole range between 0° and 180° (Figure 5d). In other words, at 300 K in the VdW stage all mutual orientations of the chlorometane and chlorine anion are possible, incuding the linear $H_3C-Cl\cdots Cl^-$ complex. This is reflected by large changes in the nonbonded C−Cl and Cl−Cl distances. In Figure 5e presented are selected snapshots of the complex at the final stage of the reaction, illustrating the above discussion.

The variety of the mutual orientations of CH_3Cl and Cl^- after C−Cl bond formation explains also the fact, that the free energy remains constant at the final stage of the reaction. The free energy profile is determined by a bond formation process; after the bond is formed, at 300 K all the orientations of chloromethane and chlorine anion are equivalent at the free energy level.

The example of the prototype SN2 reaction presented here demonstrates that the algorithm of MD along the IRP applied here works correctly also in the case of the reaction with large deviations of the molecular geometries at finite temperatures from the corresponding structures at the zero-temperature IRP.

D. $Cl-CH_2-CH=CH_2 \rightarrow CH_2=CH-CH_2Cl$ Isomerization. The last numerical example involves isomerization of 3-chloropropene (allyl chloride), in which chlorine atom is transferred between two terminal carbon atoms, through allylic TS state. The structures of the reactant, TS, and the kinetic product are shown in Figure 6a. Again, due to reactant-product symmetry, only the part of the reaction path leading from TS to a kinetic product will be discussed here.

The most stable conformation of allyl chloride is a gauche rotamer. The energy difference between gauche and cis species is 0.9 kcal/mol from our calculations. The recent experimental data[93] suggest the energy difference of 0.3−0.4 kcal/mol, while the recent RHF and MP2 calculation give the value of 0.9−1.3 kcal/mol. The gauche and cis rotamers are separated by a barrier of 2.9 kcal/mol. Here, our result reproduces the experimental value.[93] However, the IRP for the chlorine transfer reaction leads from allylic TS to the minimum corresponding to a cis conformer, which can later rotate to form a gauche species. Therefore, in the following we present the results of the MD simulation along the IRP leading to a cis rotamer.

The IRC energy and free energy profiles are shown in Figure 6b. From our calculations the free energy barrier from the 300 K MD simulation is $\Delta A^{\#} = 39.3$ kcal/mol, while the $\Delta E^{\#} = 41.8$ kcal/mol. In the case of ΔA profile an irregularity can be observed at $s = 7.5$ amu$^{-1/2}$ bohr. Namely, in this region the free energy slightly increases, to further go down to the value characterizing the product (cis rotamer); we will comment on this irregularity later.

The changes in the selected interatomic distances and the bond- and dihedral angles are shown in panels c and d of Figure 6. In the symmetric TS C−Cl bond lengths are 2.76 Å; at the 300 K they oscillate around the IRP value with a relatively large amplitude up to ±0.45 Å. The C−C distances in the allylic TS are 1.38 Å; the amplitude of their oscillations is ±0.04 Å. The zero-temperature value of the $Cl-C_1-C_2-C_3$ torsion angle is 54°, while at 300 K it oscillates between 29° and 69°. The zero-temperature values (300 K amplitudes) for the $Cl-C_1-C_2$ and $C_1-C_2-C_3$ bond angles are 84° and 117.5° (±10° and ±8.5°), respectively.

In the product, the bonded C−Cl distance is 1.83 Å, while the nonbonded one is 3.13 Å. The experimental value[93] for the bonded C−Cl distance is 1.80 Å; the previous calculations lead to a values between 1.78 and 1.80 Å. Our calculations show that at 300 K the amplitudes for the bonded and nonbonded C−Cl distances are ±0.14 and ±0.59 Å, respectively. In the product geometry, the single C−C bond length is 1.49 Å, while the double C=C bonded distance is 1.34 Å. The experimental values are 1.506 ± 0.006 Å and 1.344 ± 0.005 Å, respectively. Similarly to the previous MP2 calculations,[93] the agreement of

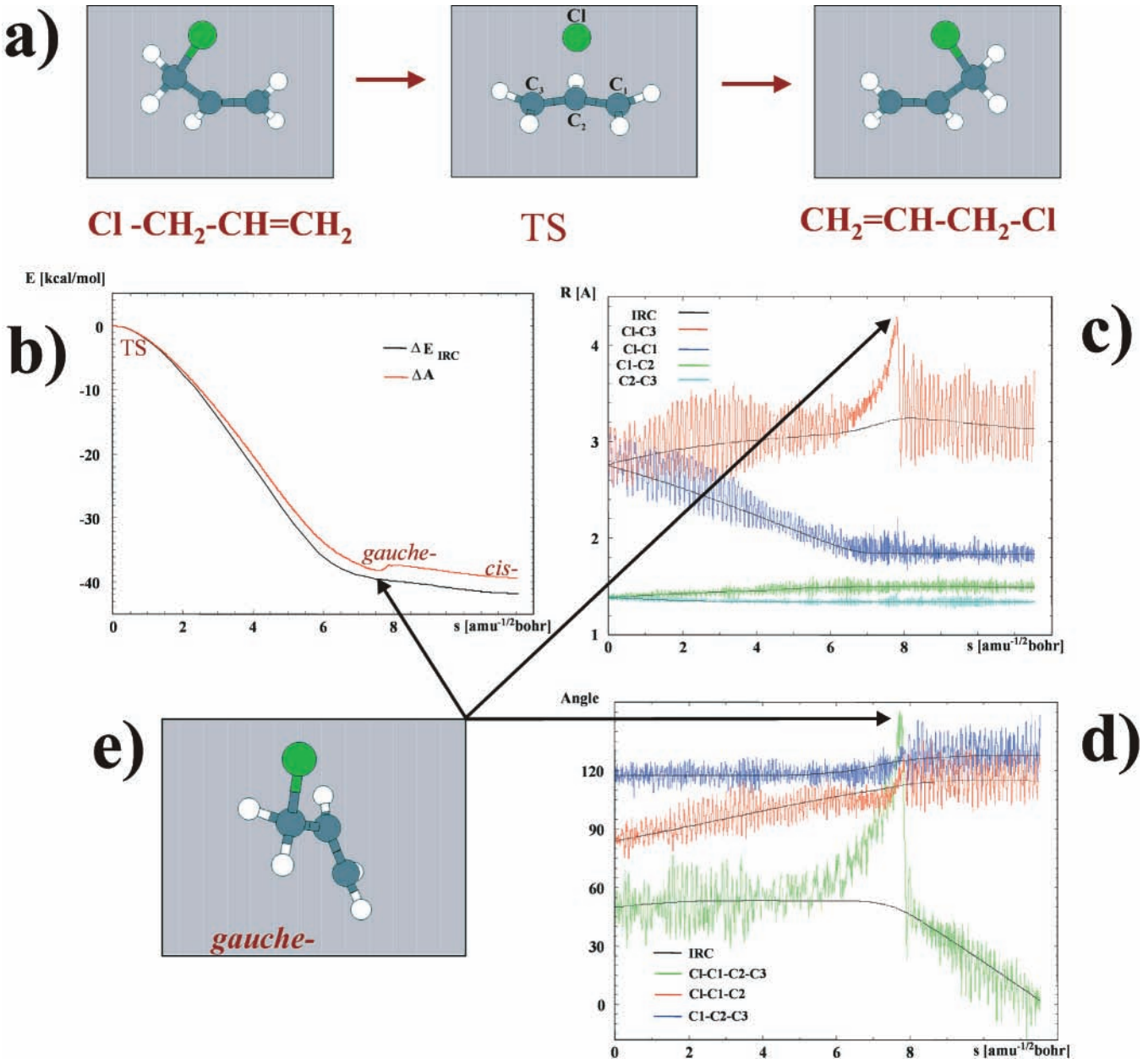

Figure 6. Isomerization of 3-chloropropene. The reactant, TS, and the product are shown in part a. Part b presents the IRC energy (black line) and the free-energy (red line) profiles. The changes in the selected interatomic distances and angles are shown in parts c and d, respectively; the black lines correspond to the changes along the IRP, while the color lines represent the changes during the 300 K MD simulation along the IRP. The geometry corresponding to the gauche rotamer (at s $\approx$ 7.8 amu$^{-1/2}$ bohr) is shown in part e.

our DFT results and the experimental values[93] is within the error bars of the latter. From our MD simulations, the amplitudes of the oscillations in the C−C distances in the product region are ±0.06 and ±0.04 Å, for the single and double bond, respectively. The Cl−C_1−C_2−C_3 torsion angle is slightly distorted from the planar orientation with the value of 1.5°; in the product region it changes with the amplitude of ±16°. The final values for the Cl−C_1−C_2 and C_1−C_2−C_3 bond angles are 114° and 127.5°, respectively; the former oscillates between 102 and 130°, while the latter between 112 and 148°. The agreement of the calculated zero-temperature values for the angles and the corresponding experimental results of 110° and 123° is reasonable. Similarly to the results of the previous HF and MP2 calculations,[93] our computed values slightly overestimate the experimental values;[93] all the computational methods give the same results, within 1°.

During the MD simulation, all the bonded interatomic distances and bond angles oscillate around their IRP values. As in the case of the free energy profile, however, in Figure 6c and 6d one can observe large deviations of the nonbonded C−Cl distance and the Cl−C_1−C_2−C_3 torsion from the corresponding IRP values in the same region of the reaction path (s = 6.0−7.8 amu$^{-1/2}$ bohr). This change in the value of the Cl−C_1−C_2−C_3 torsion reveals the origin of the irregularity in the free energy profile. Namely, despite the fact that the IRP leads from TS to the cis rotamer, at 300 K the system spontaneously evolves toward the gauche geometry. This leads to a decrease in the free energy, and is accompanied by a deviation of the nonbonded interatomic distances from their IRP values. After reaching the region with the geometry closer to the gauche rotamer, the molecule is brought back to the IRP and eventually reaches the geometry of the cis product, since the constraint used in the MD simulations forces the system to move along the IRP.

Obviously, the return of the molecule to the IRP is accompanied by a slight increase in the free-energy, as reflected by the irregularity of the profile in Figure 6b.

The chloropropene isomerization reaction represents an interesting example of the system for which MD reveals a "thermal shortcut", i.e., the 300 K path does not follow the zero-temperature IRP, leading directly to a different, more stable conformer. This example emphasizes the strength of the finite-temperature MD simulations that can often reveal the reaction paths not noticeable by the static (zero-temperature) investigations. At the same time, this example demonstrates that the algorithm used here works well even in the cases when the system geometry deviates far from the IRP during the finite-temperature simulation.

Concluding Remarks

In the present article the algorithm was presented for performing the ab initio molecular dynamics simulations along the predetermined intrinsic reaction paths. In the present work, the finite temperature MD simulations were performed with a linear constraint, freezing the system at a given point on the reaction path. The illustrative applications to simple chemical reactions show that the MD slow-growth simulations along the IRP lead to smooth free energy profiles; use of a well-defined reaction coordinate reduces problem of the free-energy hysteresis. Since the shape of the potential energy in the direction perpendicular to the reaction path changes smoothly, the slow-growth simulations along the IRP typically require less time steps than the standard approach with an a priori chosen reaction coordinate.

The illustrative examples demonstrate that the algorithm applied here works well in the cases when the reaction involves concerted changes in many geometrical parameters. The slow-growth MD along the IRP leads to smooth free-energy profiles, even when the finite-temperature paths strongly deviate from the IRP. The example of chloropropene isomerization demonstrates again, that the MD simulations can lead to discoveries of novel reaction pathways that are not noticeable from static (zero-temperature) calculations.

A similar a posteriori approach, with the use of linear constraint, can be applied for *any* predetermined reaction path defined by a set of molecular geometries., e.g., the dynamic reaction path (DRP) or simple linear-transit path.

Acknowledgment. This work has been supported by the National Sciences and Engineering Research Council of Canada (NSERC). The authors thank Dr. Serguei Patchkovskii for the helpful discussions.

References and Notes

(1) Car, R.; Parrinello, M. *Phys. Rev. Lett.* **1985**, *55*, 2471.
(2) Marx, D.; Hutter, J. In *Modern Methods and Algorithms of Quantum Chemistry*; Grotrndorst, J., Ed.; NIC Series 1; John von Neumann Institute of Computing: Jülich, 2000; pp 301−449 and references therein.
(3) Woo, T. K.; Margl, P. M.; Deng, L.; Cavallo, L.; Ziegler, T. *Catal. Today* **1999**, *50*, 479.
(4) Woo, T. K.; Margl, P. M. Deng, L. Cavallo L, Ziegler, T. In *Transition State Modeling for Catalysis*; ACS Symposium Series 721; Truhlar D. G., Morokuma, K., Eds.; American Chemical Society: Washington, DC, 1998; pp 173−186.
(5) Meier, R. J.; vanDormaele, G. H. J.; Iarlori, S.; Buda, F. *J. Am. Chem. Soc.* **1994**, *116*, 7274.
(6) Margl, P.; Schwarz, K.; Blöchl, P. E. *J. Am. Chem. Soc.* **199**4, *11*6, 11177.
(7) Margl, P.; Schwarz, K.; Blöchl, P. E. *J. Chem. Phys.* **199**5, *103*, 683.
(8) Margl, P.; Ziegler, T.; Blöchl, P. E. *J. Am. Chem. Soc.* **199**5, *117*, 12625.
(9) Margl, P.; Lohrenz, J. C. W.; Ziegler, T.; Blöchl, P. E. *J. Am. Chem. Soc.* **199**6, *118*, 4434.
(10) Woo, T.; Margl, P. M.; Lohrenz, J. C. W.; Blöchl, P. E.; Ziegler, T. *J. Am. Chem. Soc.* **1996**, *118*, 13021.
(11) Margl, P.; Ziegler, T. Blöchl, P. E. *J. Am. Chem. Soc.* **1996**, *118*, 5412.
(12) Woo, T. K.; Blöchl, P. E.; Ziegler, T. *J. Phys. Chem. A* **2000**, *104*, 121.
(13) Curioni, A.; Sprik, M.; Andreoni, W.; Schiffer, H.; Hutter, J.; Parrinello, M. *J. Am. Chem. Soc.* **1997**, *119*, 7218.
(14) Woo, T. K.; Margl, P.; Ziegler, T.; Blöchl, P. E. *Organometallics* **1997**, *16*, 3454.
(15) Margl, P. M.; Woo, T. K.; Blöchl, P.; Ziegler, T. *J. Am. Chem. Soc.* **1998**, *120*, 2174.
(16) Hutter, J.; Carloni, P.; Parrinello, M. *J. Am. Chem. Soc.* **1996**, *118*, 8710.
(17) Lamoen, D.; Parrinello, M. *Chem. Phys. Lett.* **1996**, *248*, 309.
(18) Marchi, M.; Hutter, J.; Parrinello, M. *J. Am. Chem. Soc.* **1996**, *118*, 7847.
(19) Tornaghi, M.; Andreoni, W.; Carloni, P.; Hutter, J.; Parrinello, M. *Chem. Phys. Lett.* **1995**, *246*, 469.
(20) Chan, M. S. W.; Ziegler, T. *Organometallics* **2000**. In press.
(21) Woo, T. K.; Margl, P.; Blöchl, P. E.; Ziegler, T. *J. Phys. Chem. B* **1997**, *101*, 7877.
(22) Woo, T. K. Ph.D. Thesis, University of Calgary, Calgary, 1998.
(23) Baveridge, D. L.; DiCapua, F. M. *Annu. Rev. Biophys. Chem.* **1989**, *18*, 431.
(24) Carter, E. A.; Ciccotti, G.; Hynes, J. T.; Kapral, R. *Chem. Phys. Lett.* **1989**, *156*, 472.
(25) Paci, E.; Ciccotti, G.; Ferrario, M.; Kapral, R. *Chem. Phys. Lett.* **1991**, *176*, 581.
(26) Ryckaert, J. P.; Ciccotti, G.; Berendsen, H. J. C *J. Comput. Phys.* **1977**, *23*, 327.
(27) Straatsma, T. P.; Berendsen, H. J. C.; Postma, J. P. M. *Chem. Phys.* **1986**, *85*, 6720.
(28) Fukui, K. *Acc. Chem. Res.* **1981**, *14*, 363.
(29) Tachibana, A.; Fukui, K. *Theor. Chem. Acta (Berlin)* **1980**, *57*, 81.
(30) Teketsugu, T.; Gordon, M. S. *J. Chem. Phys.* **1995**, *103*, 10042 and references therein.
(31) Ishida, K.; Morokuma, K.; Komornicki, A. J. *Chem. Phys.* **1977**, *66*, 2153.
(32) Muller, K.; Brown, L. D. *Theor. Chim. Acta (Berlin)* **1979**, *53*, 75.
(33) Garret, B. C. et al. *J. Phys. Chem.* **1988**, *92*, 1476.
(34) Gonzalez, C.; Schegel, H. B. J. *Phys. Chem.* **1990**, *94*, 5523.
(35) Deng, L. Ph.D. Thesis, University of Calgary, Calgary, 1996.
(36) Deng, L.; Ziegler. T. *Int. J. Quantum Chem.* **1994**, *52*, 731.
(37) Deng, L.; Branchedall, V.; Ziegler. T. *J. Am. Chem. Soc.* **1994**, *116*, 10645.
(38) Deng, L.; Ziegler. T. *J. Phys. Chem.* **1995**, *99*, 612.
(39) Blöchl, P. E. *Phys. Rev. B* **1994**, *50*, 17953.
(40) Blöchl, P. E. *J. Phys. Chem.* **1995**, *99*, 7422.
(41) Perdew, J. P.; Zunger, A. *Phys. Rev. B* **1981**, *23*, 5048.
(42) Becke, A. *Phys. Rev. A* **1988**, *38*, 3098.
(43) Perdew, J. P. *Phys. Rev. B* **1986**, *33*, 8822.
(44) Perdew, J. P. *Phys. Rev. B* **1986**, *34*, 7406.
(45) Nose, S. *Mol. Phys.* **1986**, *57*, 187.
(46) Hoover, W. G. *Phys. Rev. A* **1985**, *31*, 1695.
(47) Blöchl, P. E.; Parinello, M. *Phys. Rev. B* **1992**, *45*, 9413.
(48) Blöchl P. E.; Senn H. M.; Togni, A. In *Transition state Modeling for Catalysis*; ACS Symposium Series 721; Truhlar D. G., Morokuma, K., Eds.; American Chemical Society: Washington, DC, 1998; pp 88−99.
(49) Pearson, P. K.; Schaefer, H. F., III *J. Chem. Phys.* **1975**, *62*, 350.
(50) Redmon, L. T.; Purvis, G. D.; III.; Bartiett, R. J. *J. Chem. Phys.* **1980**, *72*, 986.
(51) Nobels, R. H.; Random, L. *Chem. Phys.* **1981**, *60*, 1.
(52) Peric, M.; Maledenivic, M. *Chem. Phys.* **1983**, *82*, 317.
(53) Murrell, J. N.; Carter, S. Halonen, L. O. *Mol. Spectrosc.* **1982**, *93*, 307.
(54) Holme, T. A.; Hutchinson, J. S. *J. Chem. Phys.* **1985**, *83*, 2860.
(55) Pan, C. F.; Hehre, W. J. *J. Phys. Chem.* **1982**, *86*, 321.
(56) Hehre, W. J.; Random, L.; Schleyer, P. R.; Pople, J. A. *Ab initio Molecular Orbital Theory*; Wiley: New York, 1986 and references. therein.
(57) Cooper, W.; Walters, W. D. *J. Am. Chem. Soc.* **1958**, *80*, 4220.
(58) Car, R. W., Jr.; Walters, W. D. J. *J. Phys. Chem.* **1965**, *69*, 1073.
(59) Wiberg, K. B.; Fenoglio, R. A. *J. Am. Chem. Soc.* **1968**, *90*, 3395.
(60) Lipnick, R. L.; Garbisch, E. W., Jr. *J. Am. Chem. Soc.* **1973**, *95*, 6370.
(61) Hsu, K.; Buenker, R. J.; Peyerimhoff, S. D. *J. Am. Chem. Soc.* **1971**, *93*, 2117.
(62) Hsu, K.; Buenker, R. J.; Peyerimhoff, S. D. *J. Am. Chem. Soc.* **1972**, *94*, 5639.

(63) Brulet, J.; Schaefer, H. F.; III *J. Am. Chem. Soc.* **1984**, *106*, 1221.
(64) Spellmeyer, D. C.; Houk, K. N. *J. Am. Chem. Soc.* **1988**, *110*, 3412.
(65) Bak, B.; Led, J. J.; Nygaard, L.; Rastrup-Andersen; Sorensen, G. O. *J. Mol. Struct.* **1969**, *3*, 369.
(66) Cho, Y. J.; Vande Linde, S. R.; Zhu, L.; Hase, W. L. *J. Chem. Phys.* **1992**, *96*, 8275.
(67) Barlow, S. E.; Van Doren, J. M.; Bierbaum, V. M. *J. Am. Chem. Soc.* **1988**, *110*, 7240.
(68) Mekel, A.; Havlas, Z.; Zahradnik, R. *J. Am. Chem. Soc.* **1988**, *110*, 8355.
(69) Tucker, S. C.; Truhlar, D. G. *J. Am. Chem. Soc.* **1990**, *112*, 3339.
(70) Wolfe, S.; Kim, C. K. *J. Am. Chem. Soc.* **1991**, *113*, 8056.
(71) Boyd, R. J.; Kim, C. K.; Shi, Z.; Weinberg, N.; Wolfe, S. J. *J. Am. Chem. Soc.* **1993**, *115*, 10147.
(72) Poirier, N. A.; Wang, Y.; Westaway, K. C. *J. Am. Chem. Soc.* **1994**, *116*, 2526.
(73) Certner, B. J.; Whitner, R. M.; Wilson, K. R.; Hynes, J. T. *J. Am. Chem. Soc.* **1991**, *113*, 74.
(74) Tucker, S. C.; Truhlar, D. G. *J. Am. Chem. Soc.* **1990**, *112*, 3347.
(75) Cyr, D. M.; Scarton, M. G.; Johnson, M. A. *J. Chem. Phys.* **1993**, *99*, 4869.
(76) Cyr, D. M.; Bishea G. A.; Johnson, M. A. *J. Chem. Phys.* **1992**, *97*, 5911.
(77) Dedieu, A.; Veillard, A. J. *J. Am. Chem. Soc.* **1972**, *94*, 6730.
(78) Wolfe, S.; Mitchell, D. J.; Schlegel, H. B. *J. Am. Chem. Soc.* **1981**, *103*, 7692.
(79) Wolfe, S.; Mitchell, D. J.; Schlegel, H. B. *J. Am. Chem. Soc.* **1981**, *103*, 7694.
(80) Pellerite, M. J.; Brauman, J. I. *J. Am. Chem. Soc.* **1983**, *105*, 2672.
(81) DePuy, C. H.; Gronert, S.; Mullin, A.; Bierburam, V. M. *J. Am. Chem. Soc.* **1990**, *112*, 8650.
(82) Brauman, J. I.; Olmstead, W. N.; Lieder, C. A. *J. Am. Chem. Soc.* **1974**, *96*, 4030.
(83) Keil, F.; Ahlrichs, R. *J. Am. Chem. Soc.* **1976**, *98*, 4787.
(84) Urban, M.; Cernusak, I.; Kello, V. *Chem. Phys. Lett.* **1984**, *105*, 625.
(85) Serre, J. *Int. J. Quantum Chem.* **1984**, *26*, 593.
(86) Cernusak, I.; Urban, M. *Collect. Czech. Chem. Commun.* **1988**, *53*, 2239.
(87) Wladkowski, B. D.; Lim, K. F.; Allen, W. D.; Brauman, J. I. *J. Am. Chem. Soc.* **1992**, *114*, 9136.
(88) Shi, Z.; Boyd, R. J. *J. Am. Chem. Soc.* **1989**, *111*, 1575.
(89) Vetter, R.; Zulicke, L. *J. Am. Chem. Soc.* **1990**, *112*, 5136.
(90) Tucker, S. C.; Truhlar, D. G. *J. Phys. Chem.* **1989**, *93*, 8138.
(91) Shi, Z.; Boyd, R. J. *J. Am. Chem. Soc.* **1991**, *113*, 2423.
(92) Hu, W.; Truhlar, D. G. *J. Phys. Chem.* **1994**, *98*, 1049.
(93) During, J. R.; During, D. T.; van der Veken, B. J.; Herrebout, W. A. *J. Phys. Chem. A* **1999**, *103*, 6142.